Synchronous SVM-Based Model Predictive Flux Control of Induction Motor Drives With Fast Phase Synchronization

Haitao Yang, *Member, IEEE*, Jiachen Xu, Shuo Ma, and Yongchang Zhang, *Fellow, IEEE*

***Abstract*—Synchronous space vector modulation (SSVM) has been widely applied in motor drives operated with a low switching frequency. For SSVM based closed-loop control, the phase angle of voltage command updated at each control step should equal to the predefined sampling positions. The prior arts usually adopt proportional integral controller with a sampling period compensation to achieve current regulation and phase synchronization, which show slow dynamic responses. This article proposes an SSVM-based model predictive flux control (MPFC) for induction motor drives under low switching frequency. Unlike the prior methods, which implement phase synchronization and current regulation as two cascaded control loops, the proposed MPFC achieves torque tracking control and phase synchronization simultaneously. As a result, much smaller phase error and faster synchronization speed are obtained during transient processes when compared with the prior method. Simulation and experimental tests, along with a video demonstration, justify the effectiveness of the proposed method.**

***Index Terms*—Induction motor drives, low switching frequency, model predictive control (MPC), synchronous modulation.**

I. Introduction

FOR high-power motor drives, inverters usually operate at low pulse ratio to reduce switch losses. However, traditional asynchronous modulation yields notable harmonic content in the output voltage under low pulse ratio [1]. To maintain acceptable harmonic distortions under a low switching frequency, synchronous pulsewidth modulation (PWM) schemes have been widely studied for high-power motor drives [2], [3].

Various synchronous PWM schemes, including optimized pulse pattern (OPP) [4] and synchronous space vector PWM (SSVPWM) [5], have been investigated in the existing literature. According to different optimization goal, different OPP methods, such as selective harmonic elimination PWM (SHEPWM) [6] and current harmonic minimum PWM (CHMPWM) [7], have been proposed. SHEPWM aims at eliminating some specific harmonic contents. To this end, a set of nonlinear and transcendental equations need to be solved [8]. On the contrary, CHMPWM does not try to eliminate the undesired harmonic components but focuses on minimization of the overall harmonic distortions [4]. Due to the challenge of solving nonlinear constraint optimization problem in real time on a embedded microcontroller, OPP usually computes the switching angles offline within a fundamental cycle assuming a steady state. The calculated switch angles are then stored in a lookup table for online pulse generation [9].

OPP is attractive in practical application due to its excellent steady state performance. However, the following three issues complicate the system for OPP-based closed-loop control. The first one is that current samples with OPP usually contain harmonic contents [10]. To avoid introducing excessive ripples in the control loop, either a slow current controller or online instantaneous fundamental component estimation is required [10], [11]. The second issue is that OPP is optimized within the fundamental cycle assuming a steady state, while the closed-loop controller is usually executed with a much smaller control step. The time scale mismatch of two control parts brings challenge of regulating control variables with fast dynamic responses. The third issue is that the PWM mode transition needs to be carefully designed to avoid current excursion due to different harmonic distribution among different pulse patterns of OPP [12].

The same as the conventional asynchronous SVM, SSVM generates switching pulses based on the principle of volt–second balance. However, to produce symmetrical voltage pulses, SSVM schemes have to synthesize the voltage command according to predefined sampling points and specific switching sequences [13]. As volt–second balance is satisfied within every PWM cycle, the instantaneous fundamental current can be directly measured at the start instant of each PWM interval. In addition, the magnitude and phase angle of the voltage command can be arbitrarily adjusted to achieve fast dynamic responses. Therefore, SSVM schemes have been widely applied in motor drives under a low pulse ratio [14], [15]. However, SSVM requests synchronization between the preset sampling position and phase angle of the voltage command at least during

Received 30 July 2024; revised 3 November 2024 and 1 December 2024; accepted 31 December 2024. Date of publication 6 January 2025; date of current version 26 February 2025. This work was supported in part by the National Natural Science Foundation of China under Grant 52107035, in part by Beijing Natural Science Foundation under Grant L247003, in part by the R&D Program of Beijing Municipal Education Commission under Grant KM202410009015, and in part by grants from the Delta Power Electronics Science and Education Development Program of Delta Group. Recommended for publication by Associate Editor X. Pei. *(Corresponding author: Yongchang Zhang.)*

Haitao Yang, Jiachen Xu, and Shuo Ma are with the Inverter Technologies Engineering Research Center of Beijing, North China University of Technology, Beijing 100144, China (e-mail: yhtseaky@gmail.com; 2021316280125@mail.ncut.edu.cn; 2022312080110@mail.ncut.edu.cn).

Yongchang Zhang is with the School of Electrical and Electronic Engineering, North China Electric Power University, Beijing 102206, China (e-mail: yozhang@ieee.org).

This article has supplementary material provided by the authors and color versions of one or more figures available at https://doi.org/10.1109/TPEL.2025.3525804.

Digital Object Identifier 10.1109/TPEL.2025.3525804

quasi steady state [14]. To achieve phase synchronization, the sampling period needs to be online corrected [15].

In [14], the impact of one-step delay in the phase synchronization is analyzed, and a proportional gain around 0.3 is recommended based on extensive simulation studies. It is shown that a larger gain cannot increase decay rate of the phase error, but only result in larger oscillations. In [16], a phase-locked loop (PLL) is used to adjust compensation term of the sampling period. With a PLL, the phases of voltage command can be aligned to the sampling positions of SSVM. However, the PI gains used in PLL need to be carefully tuned to avoid instability. Wang et al. [3] proposed a deadbeat phase synchronization method, which shows much faster phase synchronization. As the modulator and current controller are designed independently in the existing control system, the phase compensation regulator cannot foresee the synchronization error during transient processes. Consequently, large phase error may still be seen during transient processes with the existing methods.

During the past decades, model predictive control (MPC) has been widely investigated for motor drives [17]. When operating under low pulse ratio, long prediction horizon is essential for MPC to achieve low harmonic distortions comparable to the optimal modulation [18]. However, long horizon prediction generally leads to higher computational burden. Satisfactory steady-state performance as well as fast transient responses can also be obtained at a low switching frequency by incorporating OPPs [19], duty cycle correction [20], virtual carriers-based optimization [21], and variable applied vector numbers [22], etc.

While for SSVM-based motor drives, the proportional–integral (PI) regulator are generally used in prior studies [3], [14], [15], [16], which present relatively slower dynamic responses. Combining SSVM with MPC is rarely investigated in the existing research due to the difficulty of matching phase synchronization with quick dynamic responses of MPC. To fill this gap, a model predictive flux control (MPFC) with sampling period compensation is proposed in this article. Unlike the prior methods, which can only compensate for the phase error after it occurs, the proposed MPFC achieves phase synchronization and flux tracking control simultaneously. As a result, fast phase synchronization and dynamic responses are achieved. In addition, high-quality voltage supply of SSVM is reproduced during quasi steady state, ensuring satisfactory performance under a low switching frequency.

The rest of this article is organized as follows. Section II introduces the mathematical model of IM and its discretized model for predicting stator flux and current. The basic principle of MPFC is explained in Section III. Section IV details fundamentals of SSVM, the prior phase compensation scheme and the proposed MPFC with fast phase synchronization. The simulation and experimental results are illustrated and discussed in Section V. Finally, Section VI concludes this article.

II. Mathematical Model of IM

In the two-phase stationary reference frame, choosing stator current vector $\boldsymbol{i}_\mathrm{s}$ and stator flux vector $\boldsymbol{\psi}_\mathrm{s}$ as state variables, the mathematical model of IM can be expressed as

$$p\boldsymbol{x} = \boldsymbol{A}\boldsymbol{x} + \boldsymbol{B}\boldsymbol{u}_\mathrm{s} \tag{1}$$

$$\boldsymbol{A} = \begin{bmatrix} -\lambda(R_\mathrm{s}L_\mathrm{r} + R_\mathrm{r}L_\mathrm{s}) + j\omega_\mathrm{r} & \lambda(R_\mathrm{r} - jL_\mathrm{r}\omega_\mathrm{r}) \\ -R_\mathrm{s} & 0 \end{bmatrix} \tag{2}$$

$$\boldsymbol{B} = \begin{bmatrix} \lambda L_\mathrm{r} \\ 1 \end{bmatrix},\ \lambda = \frac{1}{L_\mathrm{s}L_\mathrm{r} - L_\mathrm{m}^2} \tag{3}$$

where p is the differential operator; $\boldsymbol{x} = [\boldsymbol{i}_\mathrm{s} \quad \boldsymbol{\psi}_\mathrm{s}]^\mathrm{T}$ are state variables; $\boldsymbol{u}_\mathrm{s}$ is the stator voltage vector; L_s, L_r, L_m, R_s, and R_r are stator inductance, rotor inductance, mutual inductance, stator resistance, and rotor resistance, respectively; ω_r is the electrical rotor speed.

To predict state variables, the Heun's method is adopted to discretize (1) for better accuracy [23], which is expressed as

$$\begin{cases} \boldsymbol{x}_\mathrm{p}^{k+1} = \boldsymbol{x}^k + t_\mathrm{s}\left(\boldsymbol{A}\boldsymbol{x}^k + B\boldsymbol{u}_\mathrm{s}^k\right) \\ \boldsymbol{x}^{k+1} = \boldsymbol{x}_\mathrm{p}^k + \frac{t_\mathrm{s}}{2}\boldsymbol{A}\left(\boldsymbol{x}_\mathrm{p}^{k+1} - \boldsymbol{x}^k\right) \end{cases} \tag{4}$$

where the superscript k represents variables at the current sampling instant and $k+1$ denotes the first sampling instant in the future; $\boldsymbol{x}^{k+1} = [\ \boldsymbol{i}_\mathrm{s}^{k+1} \quad \boldsymbol{\psi}_\mathrm{s}^{k+1}\ ]^\mathrm{T}$ is the predicted state variables of stator current and stator flux at $(k+1)$th sampling instant; t_s is the sampling period.

After obtaining the predicted stator current $\boldsymbol{i}_\mathrm{s}^{k+1}$ and stator flux $\boldsymbol{\psi}_\mathrm{s}^{k+1}$ according to (4), the rotor flux $\boldsymbol{\psi}_\mathrm{r}^{k+1}$ can be estimated as

$$\boldsymbol{\psi}_\mathrm{r}^{k+1} = \frac{L_\mathrm{r}}{L_\mathrm{m}}\boldsymbol{\psi}_\mathrm{s}^{k+1} - \frac{1}{\lambda L_\mathrm{m}}\boldsymbol{i}_\mathrm{s}^{k+1}. \tag{5}$$

The electromagnetic torque is a cross product of stator flux and rotor flux vector, which is expressed as

$$\begin{aligned} T_\mathrm{e} &= \frac{3}{2}N_\mathrm{p}\lambda L_\mathrm{m}\left|\boldsymbol{\psi}_\mathrm{r} \otimes \boldsymbol{\psi}_\mathrm{s}\right| \\ &= \frac{3}{2}N_\mathrm{p}\lambda L_\mathrm{m}\left|\boldsymbol{\psi}_\mathrm{r}\right|\left|\boldsymbol{\psi}_\mathrm{s}\right|\sin\left(\angle\boldsymbol{\psi}_\mathrm{s} - \angle\boldsymbol{\psi}_\mathrm{r}\right) \end{aligned} \tag{6}$$

where $\otimes$ denotes the cross product of two complex variables, $|\ |$ represents the magnitude of a complex variable, and N_p is the number of pole pairs, respectively.

III. Basic Principle of MPFC

In practical application, it is difficult to measure the flux information within the motor directly. To estimate stator flux with a good accuracy over a wide speed range, the full-order observer is adopted in this article and its mathematical model is expressed as

$$p\hat{\boldsymbol{x}} = \boldsymbol{A}\hat{\boldsymbol{x}} + \boldsymbol{B}\boldsymbol{u}_\mathrm{s} + \boldsymbol{G}\left(\boldsymbol{i}_\mathrm{s} - \hat{\boldsymbol{i}}_\mathrm{s}\right) \tag{7}$$

$$\boldsymbol{G} = -\begin{bmatrix} 2b \\ \dfrac{b}{\lambda L_\mathrm{r}} \end{bmatrix} \tag{8}$$

where $\hat{\boldsymbol{x}} = [\hat{\boldsymbol{i}}_\mathrm{s} \quad \hat{\boldsymbol{\psi}}_\mathrm{s}]^\mathrm{T}$ are estimated state variables; $\boldsymbol{G}$ shown in (8) is a gain vector; $b < 0$ represents that the observer poles are left shifted on the complex plane by a distance b relative to the motor model [23].

According to (6), the phase angle of stator flux vector can be derived as [23]

$$\angle\boldsymbol{\psi}_{\mathrm{s}}^{\mathrm{ref}} = \angle\boldsymbol{\psi}_{\mathrm{r}}^{k+1} + \theta_{\mathrm{T}}^{k+1} \tag{9}$$

$$\theta_{\mathrm{T}}^{k+1} = \mathrm{asin}\left(\frac{2T_{\mathrm{e}}^{\mathrm{ref}}}{3N_p\lambda L_m\left|\boldsymbol{\psi}_{\mathrm{r}}^{k+1}\right|\psi_{\mathrm{s}}^{\mathrm{ref}}}\right) \tag{10}$$

where asin() is the inverse sine function, $T_{\mathrm{e}}^{\mathrm{ref}}$ is the torque reference, and $\psi_{\mathrm{s}}^{\mathrm{ref}}$ is the stator flux amplitude reference.

Due to the one-step delay in digital control system, the voltage command is updated and applied during the next control period. To compensate for the delay, the stator flux reference at the $(k+2)$th sampling instant should be calculated based on (9) as

$$\angle\boldsymbol{\psi}_{\mathrm{s}}^{\mathrm{ref}} = \angle\boldsymbol{\psi}_{\mathrm{r}}^{k+2} + \theta_{\mathrm{T}}^{k+2}. \tag{11}$$

The rotor flux linkage vector $\boldsymbol{\psi}_{\mathrm{r}}^{k+2}$ can be predicted by shifting (4) and (5) one-step ahead further. For simplicity, this article extrapolates $\boldsymbol{\psi}_{\mathrm{r}}^{k+2}$ as

$$\boldsymbol{\psi}_{\mathrm{r}}^{k+2} = \boldsymbol{\psi}_{\mathrm{r}}^{k+1}e^{j\omega_{\mathrm{e}}t_{\mathrm{s}}^{k+1}} \tag{12}$$

where ω_{e} represents the rotational angular velocity of the rotor flux linkage vector. In this article, ω_{e} is calculated as

$$\omega_{\mathrm{e}} = \omega_{\mathrm{r}} + \omega_{\mathrm{sl}} = \omega_{\mathrm{r}} + \frac{2R_{\mathrm{r}}T_{\mathrm{e}}^{k+1}}{3N_{\mathrm{p}}\left|\boldsymbol{\psi}_{\mathrm{r}}^{k+1}\right|^2} \tag{13}$$

where ω_{sl} denotes the slip frequency.

The rotor flux angle $\angle\boldsymbol{\psi}_{\mathrm{r}}^{k+2}$ can then be calculated as

$$\angle\boldsymbol{\psi}_{\mathrm{r}}^{k+2} = \angle\boldsymbol{\psi}_{\mathrm{r}}^{k+1} + \omega_{\mathrm{e}}t_{\mathrm{s}}^{k+1}. \tag{14}$$

The reference of the stator flux vector can be constructed based on its amplitude and phase angle as

$$\boldsymbol{\psi}_{\mathrm{s}}^{\mathrm{ref}} = \psi_{\mathrm{s}}^{\mathrm{ref}}e^{j\angle\boldsymbol{\psi}_{\mathrm{s}}^{\mathrm{ref}}}. \tag{15}$$

After getting $\boldsymbol{\psi}_{\mathrm{s}}^{\mathrm{ref}}$, the voltage command is calculated as

$$\boldsymbol{u}_{\mathrm{s}}^{\mathrm{ref}} = \frac{\boldsymbol{\psi}_{\mathrm{s}}^{\mathrm{ref}} - \boldsymbol{\psi}_{\mathrm{s}}^{k+1}}{t_{\mathrm{s}}^{k+1}} + R_{\mathrm{s}}\boldsymbol{i}_{\mathrm{s}}^{k+1}. \tag{16}$$

IV. Phase Synchronization for SSVM-Based MPFC

A. Introduction of SSVM

A three-phase two-level voltage inverter can generate eight voltage vectors, comprising six different active vectors and two zero vectors. The six active vectors divide the complex plane into six sectors, as shown in Fig. 1.

Based on the principle of volt–second balance, the voltage vectors in each sector can be synthesized by the two adjacent active vectors and zero vectors. For example, if the voltage reference locates in the sector I, the duration of voltage vector $\boldsymbol{u}_{1,2}$ and the zero-voltage vector can be calculated as

$$\begin{cases} t_1 = \frac{2\sqrt{3}}{\pi}Mt_{\mathrm{s}}\sin\left(\pi/3 - \theta_{\mathrm{u}}\right) \\ t_2 = \frac{2\sqrt{3}}{\pi}Mt_{\mathrm{s}}\sin\theta_{\mathrm{u}} \\ t_0 = t_{\mathrm{s}} - t_1 - t_2 \end{cases} \tag{17}$$

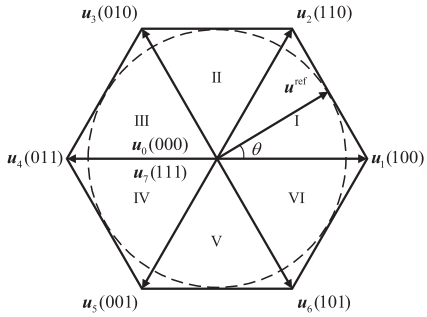

Fig. 1. Voltage vectors and switching states produced by a two-level three-phase inverter.

TABLE I
SSVM and Their Corresponding Sampling Positions in Sector I

P	N	Sampling position	Vector sequence
15	5	6°, 18°, 30°, 42°, 54°	0127, 7210, 0127, 7210, 0127
11	5	6°, 18°, 30°, 42°, 54°	012, 210, 0127, 721, 127
7	3	10°, 30°, 50°	127, 7210, 012
5	2	15°, 45°	012, 127

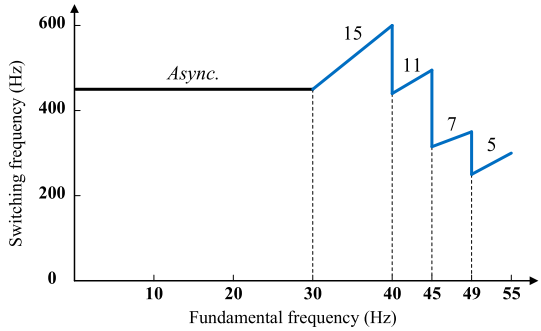

Fig. 2. Relationship between the PWM method and fundamental frequency.

where $t_{0,1,2}$ are action time of zero-voltage vector and active vectors $\boldsymbol{u}_{1,2}$, respectively; $M = \pi|\boldsymbol{u}_{\mathrm{s}}^{\mathrm{ref}}|/(2u_{\mathrm{dc}})$ is the modulation index; u_{dc} is the dc bus voltage and $\theta_{\mathrm{u}} = \angle\boldsymbol{u}_{\mathrm{s}}^{\mathrm{ref}}$ is the phase of the voltage command.

To meet the conditions of three-phase symmetry, half-wave symmetry, and quadrature-wave symmetry, SSVMs have to generate the switching pulses based on specific vector sequences and sampling positions [5]. In this article, the conventional space vector strategy (CSVS) with a pulse ratio of $P = 15$, the basic bus clamping strategy-I (BBCS-I) with pulse ratios of $P = \{11, 7\}$ and the basic bus clamping strategy-II (BBCS-II) with a pulse ratio of $P = 5$ are selected. For convenience, they are referred to as CSVS_15, BBCS_11, BBCS_7, and BBCS_5 in the following text. The sampling positions and corresponding switching sequences are listed in Table I [5], [13]. To limit the maximum switching frequency, different SSVM schemes are applied over the full speed range, as shown in Fig. 2.

B. Prior Phase Synchronization

In ideal conditions, the phase of the voltage command should strictly coincide with the sampling positions set by the SSVM

scheme. However, in a closed-loop control system, the phase of the voltage command may be adjusted arbitrarily by the controller at any time, making it difficult to ensure consistence between the phase of the voltage command and the predefined sampling positions.

In [14] and [15], a method to correct the sampling period is developed to suppress phase synchronization errors. The sampling period compensation term t_{c} is calculated based on the phase synchronization error as

$$t_{\mathrm{c}}^{k+1} = \alpha \frac{\left(\theta_{\mathrm{r}}^{k} - \theta_{\mathrm{u}}^{k}\right)}{2\pi f_{\mathrm{e}}} \tag{18}$$

where θ_{u} represents the phase angle of the voltage command; θ_{r} denotes the sampling position; f_{e} is the fundamental frequency; α is the compensation gain.

For SSVM schemes, there are N samples in each sector, amounting to $6N$ sampling positions within six sectors. Without losing generality, the sampling positions of an SSVM method can be expressed as

$$\theta_{\mathrm{r}} = m\frac{2\pi}{6N} + \theta_0 \tag{19}$$

where $m \in \{0, 1, \ldots, 6N-1\}$ represents the mth sampling positions and θ_0 is the first sampling position. As $6N$ sampling positions are evenly distributed on the complex plane, the sampling period without any correction should be

$$t_{\mathrm{s0}} = \frac{1}{6Nf_{\mathrm{e}}}. \tag{20}$$

With the compensation term calculated based on (18), the actual sampling period is

$$t_{\mathrm{s}}^{k+1} = t_{\mathrm{s0}} + t_{\mathrm{c}}^{k+1}. \tag{21}$$

As it can be seen from (18), the compensation value of the next sampling period is calculated based on the kth instant phase error $\Delta\theta_{\mathrm{u}}^{k} = \theta_{\mathrm{r}}^{k} - \theta_{\mathrm{u}}^{k}$. Such one-step delay deteriorates dynamic responses of the phase synchronization and may even cause instability if phase compensation loop is not properly designed and tuned. In [14], $\alpha = 0.3$ is suggested to achieve the best performance.

C. MPFC With Fast Phase Synchronization

For the prior compensation method, the sampling period correction and closed-loop controller operate independently. The phase error decay rate is limited to ensure stability and large phase error may be seen when the torque reference suddenly changes. To address the above issues, this article proposes an improved method to calculate the sampling period compensation term t_{c}^{k+1}. With the proposed method, the phase synchronization and flux linkage vector tracking are achieved simultaneously.

The overall block diagram of the proposed method is shown in Fig. 3. The rotor speed is regulated by a PI controller, which generates the torque reference $T_{\mathrm{e}}^{\mathrm{ref}}$. The stator flux is estimated using a full-order observer as mentioned in Section III. The torque and flux amplitude references are equivalently transformed into the reference of the stator flux vector based on (9)–(15). Then, the voltage command and sampling period compensation value

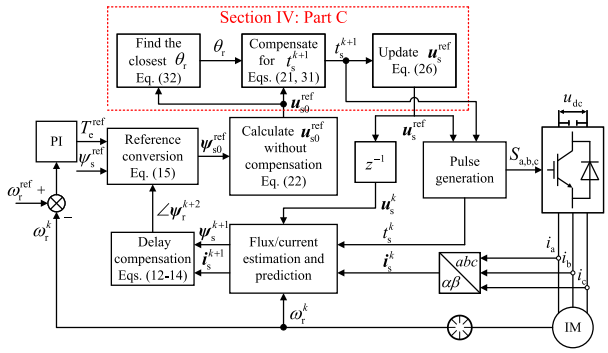

Fig. 3. Control diagram of SSVM-based MPFC.

are calculated with the proposed MPFC. After that, the vector duration is calculated based on (17). Finally, the gate pulses can be generated using the SSVM listed in Table I.

According to the MPFC described in Section III, the voltage reference without sampling period compensation can be solved based on (11)–(16) as

$$\begin{cases} \angle\boldsymbol{\psi}_{\mathrm{s0}}^{\mathrm{ref}} = \angle\boldsymbol{\psi}_{\mathrm{r}}^{k+1} + \omega_{\mathrm{e}} t_{\mathrm{s0}} + \theta_{\mathrm{T}}^{k+2} \\ \boldsymbol{\psi}_{\mathrm{s0}}^{\mathrm{ref}} = \psi_{\mathrm{s}}^{\mathrm{ref}} e^{j\angle\boldsymbol{\psi}_{\mathrm{s0}}^{\mathrm{ref}}} \\ \boldsymbol{u}_{\mathrm{s0}}^{\mathrm{ref}} = \dfrac{\boldsymbol{\psi}_{\mathrm{s0}}^{\mathrm{ref}} - \boldsymbol{\psi}_{\mathrm{s}}^{k+1}}{t_{\mathrm{s0}}} + R_{\mathrm{s}}\boldsymbol{i}_{\mathrm{s}}^{k+1} \end{cases} \tag{22}$$

where $\boldsymbol{\psi}_{\mathrm{s0}}^{\mathrm{ref}}$ and $\boldsymbol{u}_{\mathrm{s0}}^{\mathrm{ref}}$ denote references of the stator flux vector and stator voltage vector without sampling period compensation. The voltage reference calculated from (22) can guarantee accurate flux tracking, but the phase angle of the voltage reference may not coincide with the predefined sampling positions. To address this issue, a compensation term t_{c}^{k+1} is added to t_{s0}.

With a sampling period compensation term t_{c}^{k+1}, the phase angle of rotor flux at $(k+2)$th sampling instant can be derived based on (14) and (21) as

$$\begin{aligned} \angle\boldsymbol{\psi}_{\mathrm{r}}^{k+2} &= \angle\boldsymbol{\psi}_{\mathrm{r}}^{k+1} + \omega_{\mathrm{e}} t_{\mathrm{s0}} + \omega_{\mathrm{e}} t_{\mathrm{c}}^{k+1} \\ &= \angle\boldsymbol{\psi}_{\mathrm{r0}}^{k+2} + \omega_{\mathrm{e}} t_{\mathrm{c}}^{k+1} \end{aligned} \tag{23}$$

where $\angle\boldsymbol{\psi}_{\mathrm{r0}}^{k+2} = \angle\boldsymbol{\psi}_{\mathrm{r}}^{k+1} + \omega_{\mathrm{e}} t_{\mathrm{s0}}$ represents the rotor flux angle without compensation. Then, the compensated reference value of the stator flux vector and its phase can be obtained based on (11) and (15) as

$$\begin{aligned} \angle\boldsymbol{\psi}_{\mathrm{s}}^{\mathrm{ref}} &= \angle\boldsymbol{\psi}_{\mathrm{r}}^{k+2} + \theta_{\mathrm{T}}^{k+2} = \angle\boldsymbol{\psi}_{\mathrm{r0}}^{k+2} + \theta_{\mathrm{T}}^{k+2} + \omega_{\mathrm{e}} t_{\mathrm{c}}^{k+1} \\ &= \angle\boldsymbol{\psi}_{\mathrm{s0}}^{\mathrm{ref}} + \omega_{\mathrm{e}} t_{\mathrm{c}}^{k+1} \end{aligned} \tag{24}$$

$$\boldsymbol{\psi}_{\mathrm{s}}^{\mathrm{ref}} = \psi_{\mathrm{s}}^{\mathrm{ref}} e^{j\left(\angle\boldsymbol{\psi}_{\mathrm{s0}}^{\mathrm{ref}} + \omega_{\mathrm{e}} t_{\mathrm{c}}^{k+1}\right)} = \boldsymbol{\psi}_{\mathrm{s0}}^{\mathrm{ref}} e^{j\omega_{\mathrm{e}} t_{\mathrm{c}}^{k+1}}. \tag{25}$$

According to (16) and (21), the voltage command with sampling period compensation can be calculated as

$$\boldsymbol{u}_{\mathrm{s}}^{\mathrm{ref}} = \frac{\boldsymbol{\psi}_{\mathrm{s0}}^{\mathrm{ref}} e^{j\omega_{\mathrm{e}} t_{\mathrm{c}}^{k+1}} - \boldsymbol{\psi}_{\mathrm{s}}^{k+1}}{t_{\mathrm{s0}} + t_{\mathrm{c}}^{k+1}} + R_{\mathrm{s}}\boldsymbol{i}_{\mathrm{s}}^{k+1}. \tag{26}$$

The SSVM is usually applied during medium and high speed ranges. Hence, when SSVM is applied, the impact of voltage drop on the stator resistance is of minor importance [19].

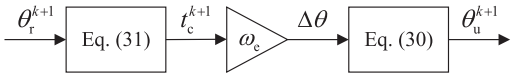

Fig. 4. Block diagram of phase synchronization.

Neglecting the term $R_s \boldsymbol{i}_s^{k+1}$ and letting $\Delta\theta = \omega_e t_c^{k+1}$, $\boldsymbol{u}_s^{ref}$ expressed in (26) can be rearranged as

$$\boldsymbol{u}_s^{ref} \approx \frac{\omega_e \left[\psi_s^{ref} e^{j(\angle \boldsymbol{\psi}_{s0}^{ref} + \Delta\theta)} - \boldsymbol{\psi}_s^{k+1}\right]}{\pi/(3N) + \Delta\theta}. \tag{27}$$

The real part and imaginary part of the complex vector $\boldsymbol{u}_s^{ref}$ can be derived from (27) as

$$u_{s\alpha}^{ref} = \frac{\omega_e \left[\psi_s^{ref} \cos\left(\angle \boldsymbol{\psi}_{s0}^{ref} + \Delta\theta\right) - \psi_{s\alpha}^{k+1}\right]}{\pi/(3N) + \Delta\theta} \tag{28}$$

$$u_{s\beta}^{ref} = \frac{\omega_e \left[\psi_s^{ref} \sin\left(\angle \boldsymbol{\psi}_{s0}^{ref} + \Delta\theta\right) - \psi_{s\beta}^{k+1}\right]}{\pi/(3N) + \Delta\theta} \tag{29}$$

where $\psi_{s\alpha}$ and $\psi_{s\beta}$ represent the real and imaginary parts of stator flux vector $\boldsymbol{\psi}_s$.

Based on (28) and (29), the phase angle of $\boldsymbol{u}_s^{ref}$ can be derived as

$$\angle \boldsymbol{u}_s^{ref} = \text{atan}\left[\frac{\psi_s^{ref} \sin\left(\angle \boldsymbol{\psi}_{s0}^{ref} + \Delta\theta\right) - \psi_{s\beta}^{k+1}}{\psi_s^{ref} \cos\left(\angle \boldsymbol{\psi}_{s0}^{ref} + \Delta\theta\right) - \psi_{s\alpha}^{k+1}}\right] \tag{30}$$

where atan() is the inverse tangent function.

According to the derivation process attached in the Appendix, solving (30) for t_c^{k+1} to make $\angle \boldsymbol{u}_s^{ref}$ equal to a sampling position θ_r^{k+1} yields

$$t_c^{k+1} = \frac{\theta_r - \angle \boldsymbol{\psi}_{s0}^{ref} - \text{asin}\left[\frac{\boldsymbol{\psi}_s^{k+1} \otimes e^{j\theta_r^{k+1}}}{\psi_s^{ref}}\right]}{\omega_e}. \tag{31}$$

It should be noted that the phase synchronization is only required when SSVM is implemented, which generally operates at medium and high speed ranges. Hence, there is no issue to divide phase error by ω_e. In practical application, an overlarge t_c^{k+1} is unfavorable. To ensure that the control algorithm can be completed within one sampling period while not impairing dynamic responses, t_c^{k+1} is limited within the range of $-0.5t_{s0} \le t_c^{k+1} \le 0.5t_{s0}$.

To minimize t_c^{k+1}, the sampling position θ_r closest to $\boldsymbol{u}_s^{ref}$ should be found, which can be derived according to (19) as

$$\begin{cases} m = \text{round}\left(\frac{3N}{\pi}\left[\angle \boldsymbol{u}_{s0}^{ref} - \theta_0\right]\right) \\ \theta_r = \frac{m\pi}{3N} + \theta_0 \end{cases} \tag{32}$$

where round() is the function used to round a number to the nearest integer. After obtaining t_c^{k+1}, the sampling period t_s^{k+1} and the voltage command can be reconstructed according to (21) and (26).

According to (27)–(31), the block diagram of the phase synchronization loop is illustrated in Fig. 4. Based on (31), the compensated phase $\Delta\theta$ is calculated as

$$\Delta\theta = \omega_e t_c^{k+1} = \theta_r^{k+1} - \angle \boldsymbol{\psi}_{s0}^{ref} - \text{asin}\left[\frac{\psi_{s\alpha}^{k+1} \sin(\theta_r^{k+1}) - \psi_{s\beta}^{k+1} \cos(\theta_r^{k+1})}{\psi_s^{ref}}\right]. \tag{33}$$

Substituting $\Delta\theta$ into (30) yields

$$\theta_u^{k+1} = \text{atan}\left(\frac{\sin(\theta_r^{k+1})}{\cos(\theta_r^{k+1})} \frac{\psi_s^{ref} \cos(\theta_x) - \boldsymbol{\psi}_s^{k+1} \odot e^{j\theta_r^{k+1}}}{\psi_s^{ref} \cos(\theta_x) - \boldsymbol{\psi}_s^{k+1} \odot e^{j\theta_r^{k+1}}}\right) = \theta_r^{k+1} \tag{34}$$

where $\odot$ denotes the dot product of two complex variables, and θ_x is expressed as

$$\theta_x = \text{asin}\left(\frac{\boldsymbol{\psi}_s^{k+1} \otimes e^{j\theta_r^{k+1}}}{\psi_s^{ref}}\right). \tag{35}$$

It can be seen from (34) that the proposed method can align the phase angle of the voltage command to the preset sampling position. The transfer function from θ_r to θ_u is

$$F(z) = \frac{\theta_r(z)}{\theta_u(z)} = 1. \tag{36}$$

Apparently, the phase synchronization loop is always stable. To illustrate the implementation process of the proposed method more clearly, a flowchart of the developed algorithm is shown in Fig. 5.

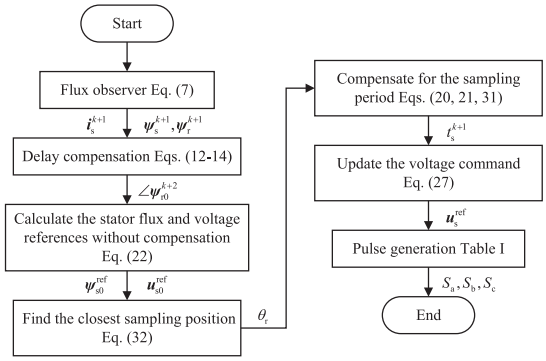

Fig. 5. Flowchart of the proposed method.

V. Simulation and Experimental Tests

To validate the effectiveness of the proposed method, simulation tests with a 180-kW IM drive and experimental tests with a down-scaled 2.2 kW IM drive were carried out. The parameters of the IMs are presented in Table II. Below 30 Hz, the conventional asynchronous SVM is applied and SSVM schemes listed in Table I are applied at higher speeds, as shown in Fig. 2. For comparison, the prior sampling period compensation methods developed in [3], [14], and [16] are also implemented. In the following text, they are referred to as the prior method I, the prior method II, and the prior method III, respectively.

TABLE II
PARAMETERS OF TESTED IMS

Rated power	P_n	2.2 kW	180 kW
DC-bus voltage	U_{dc}	540 V	1100 V
Rated voltage	U_n	380 V	1100 V
Rated frequency	f_n	50 Hz	60 Hz
Number of pole pairs	N_p	2	2
Stator resistance	R_s	3.126 Ω	0.009 Ω
Rotor resistance	R_r	1.879 Ω	0.065 Ω
Mutual inductance	L_m	0.221 H	0.038 H
Stator inductance	L_s	0.2301 H	0.0394 H
Rotor inductance	L_r	0.2301 H	0.0397 H

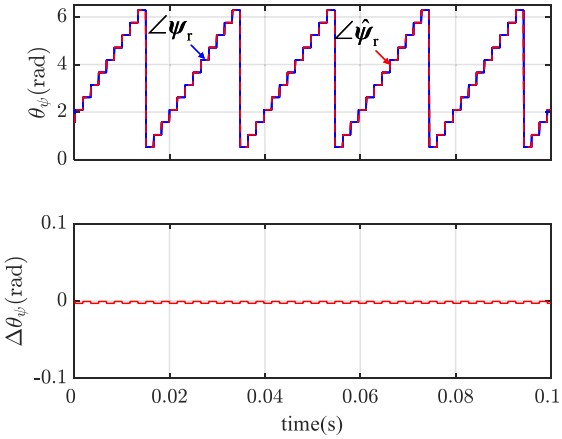

Fig. 6. Simulated responses of the predicted phase angle of the rotor flux linkage vector.

A. Simulation Results

Simulation tests were implemented in the environment of Matlab/Simulink. In the figure, the phase angle of the voltage command θ_u has been wrapped into the range of $[0, \pi/3]$ for easy comparison with the sampling positions listed in Table I.

Fig. 6 illustrates responses of the actual phase angle of the rotor flux linkage vector and its predicted value based on (14). As the $\angle\hat{\psi}_r$ is a predicted value at the $(k+2)$th instant, it is delayed by two sampling instants for comparison with the actual value $\angle\psi_r$. It can be seen that the prediction error is nearly zero, justifying satisfactory accuracy of the rotor flux linkage prediction based on (14).

Fig. 7 shows the simulated responses when the torque references suddenly increases from 0 to 560 N · m with BBCS_11. It is seen that the actual torque can track its reference quickly with a settling time around 2 ms using SSVM-based MPFC. In the figure, $\Delta\theta_u = \theta_u - \theta_r$ denotes the phase synchronization error. It is seen that all methods can achieve phase synchronization during steady state, except that the prior method II presents some minor oscillating error components. During transients, the phase angle of the voltage command θ_u deviates from the preset sampling positions obviously with the prior compensation methods, and it takes relatively longer time for $\Delta\theta_u$ to recover to zero. On the contrary, the proposed MPFC can adjust the sampling period timely to prevent the occurrence of a large phase error.

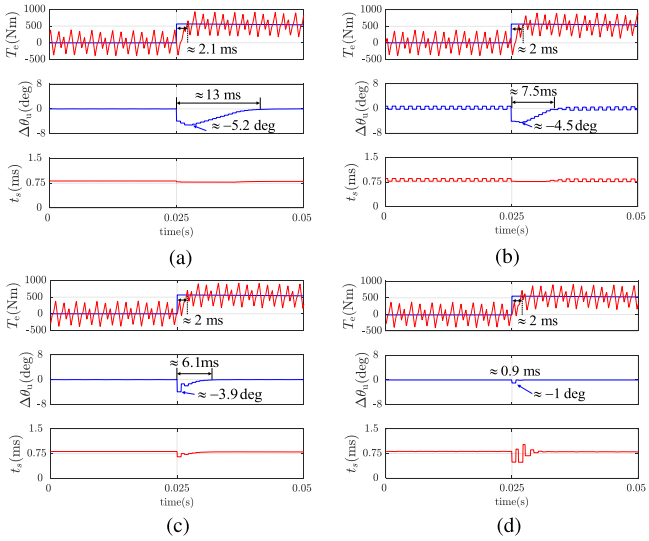

Fig. 7. Simulated responses when the torque reference steps with different sampling period compensation methods. (a) With the prior method I. (b) With the prior method II. (c) With the prior method III. (d) With the proposed method.

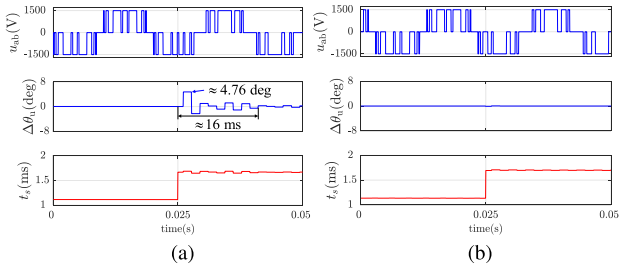

Fig. 8. Simulated responses during PWM mode transition. (a) With the prior method I. (b) With the proposed method.

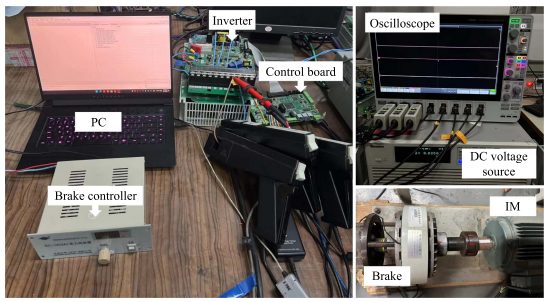

Fig. 9. Experimental test rig.

Fig. 8 shows transition process when the SSVM changes from BBCS_7 to BBCS_5. It is found that the prior compensation method shows obvious phase synchronization error during PWM mode transition. A relatively longer time is required for suppressing the phase error, while the proposed method is almost not affected during the whole process. This test further confirms good transient performance of the proposed method.

B. Experimental Results

To further verify the effectiveness of the proposed method, experimental tests were evaluated on a down-scaled two-level

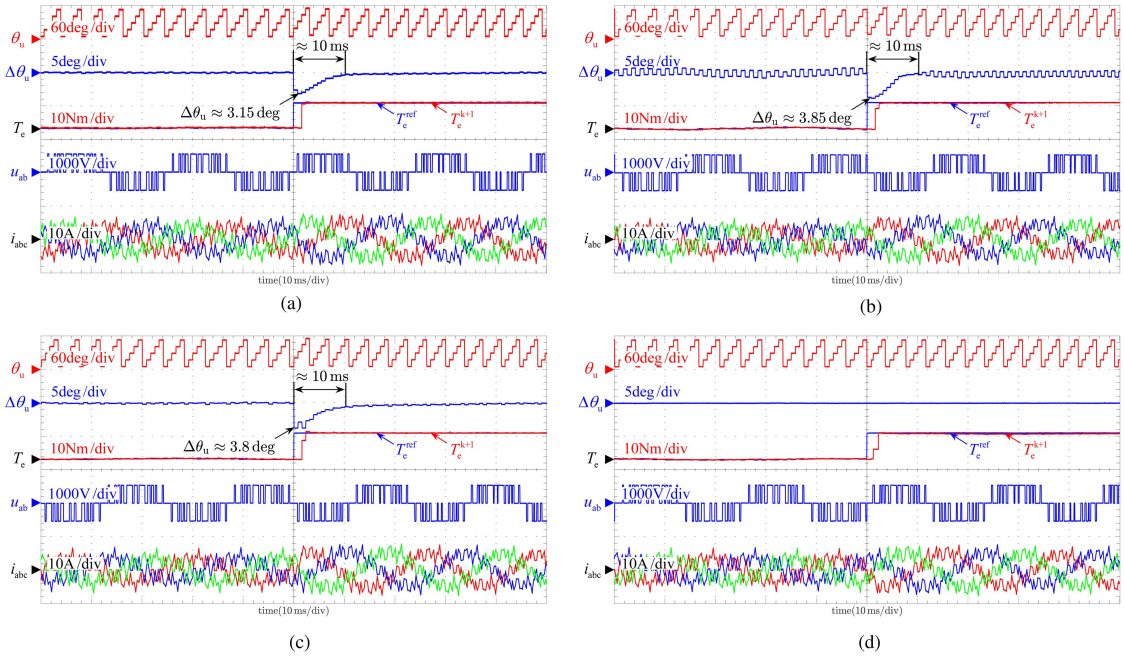

Fig. 10. Experimental results with a step change of the torque reference under BBCS_11. (a) With the prior method I. (b) With the proposed method II. (c) With the prior method III. (d) With the proposed method.

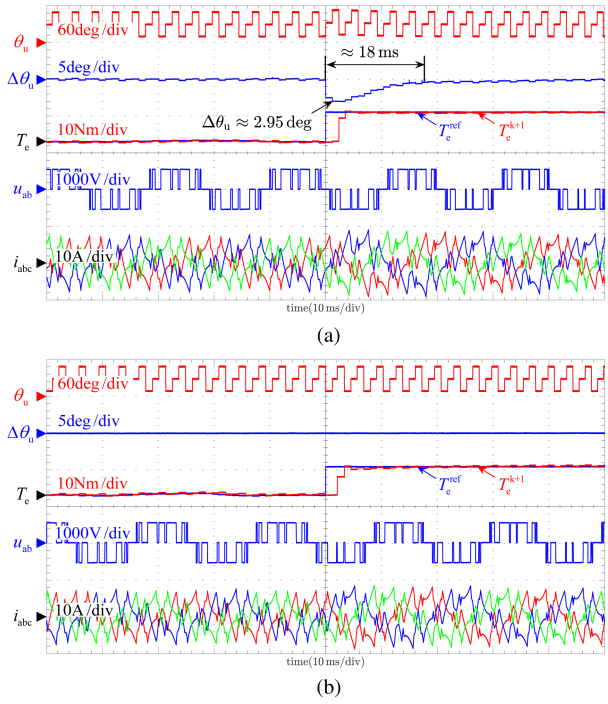

Fig. 11. Experimental results with a step change of the torque reference under BBCS_7. (a) With the prior method I. (b) With the proposed method.

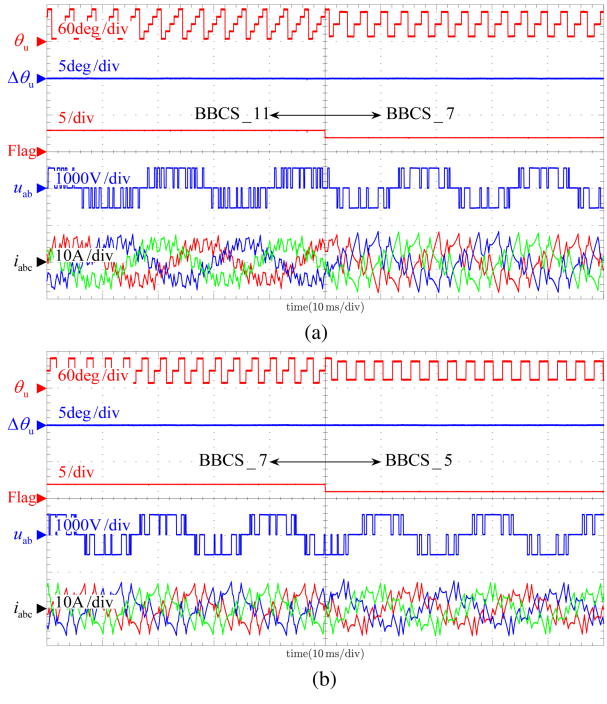

Fig. 12. Experimental results during PWM mode transition with the proposed MPFC. (a) From BBCS_11 to BBCS_7. (b) From BBCS_7 to BBCS_5.

inverter fed 2.2-kW IM drive, as shown in Fig. 9. The motor parameters are listed in Table II. The control algorithm was coded in C language and implemented with a 32-bit floating point DSP TMS320F28335. Apart from three-phase currents and line voltage, which are directly measured by probes, the other variables are displayed on an 8-channel oscilloscope MOS58 via a digital-to-analog converter.

Fig. 10 shows the responses when the torque reference suddenly increases to the rated value under BBCS_11 with different phase synchronization methods. In all tests, the torque

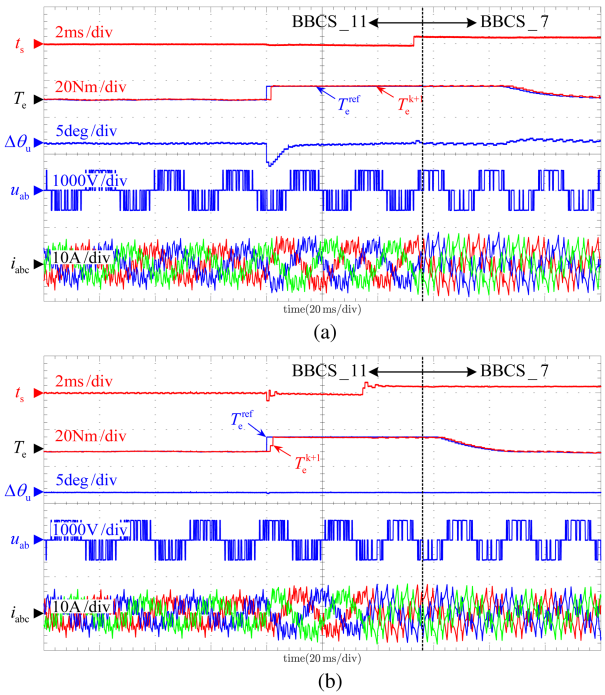

Fig. 13. Responses during speed acceleration processes. (a) With the prior method I. (b) With the proposed method.

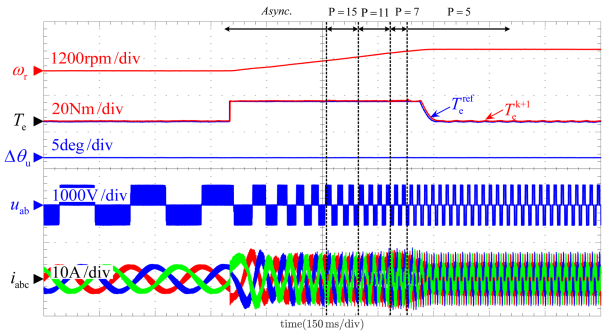

Fig. 14. Responses when the motor accelerates from 5 Hz to the rated speed with the proposed method.

can track its reference quickly. However, MPFC with the prior time compensation shows larger phase synchronization error and slow error decay rate. Similar to the simulation results in Fig. 7, the average phase synchronization error is zero during steady state for the prior method II, but the oscillating error components are relatively larger. By contrast, the phase synchronization is well kept with the proposed MPFC, which is almost not affected by sudden change of the torque reference. The results validate that the proposed MPFC can achieve fast dynamic responses and accurate phase synchronization based on SSVM.

Fig. 11 shows the responses when the torque reference suddenly increases under BBCS_7 for the prior method I and the proposed method. Both methods can keep phase synchronization under steady state. The proposed method can eliminate synchronization error even during fast torque transients while

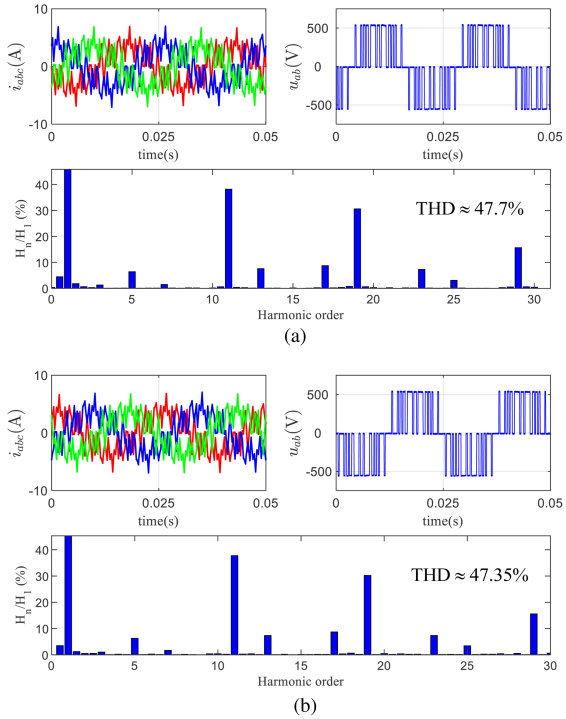

Fig. 15. Experimental results of stator current, line voltage and spectrum of a-phase current. (a) BBCS_11 with the prior method. (b) BBCS_11 with the proposed method.

the prior method presents larger phase error and around 18 ms is consumed for resynchronization.

Fig. 12 shows the responses during SSVM mode transition with the proposed MPFC. Similar to the simulation results, the proposed method achieves smooth transition between different SSVM schemes. The voltage phase θ_u is consistent with the predefined sampling positions and the phase error is nearly zero. The line voltage pulses are thus kept symmetry under steady state. Similar results can be obtained for transitions between other SSVM schemes, and thus they are not illustrated for conciseness.

Fig. 13 illustrates the test results during speed acceleration process. When there is a step change in torque reference or a PWM mode transition, the prior method shows obvious phase deviation. Then, a relatively longer time is consumed to suppress the phase error. By comparison, the proposed method can adjust the sampling period timely to prevent occurrence of the synchronization error. As can be seen from Fig. 13(b), the phase error is kept at zero without being influenced by the varying torque and PWM mode transition.

Fig. 14 illustrates the responses when the motor accelerates from 5 Hz to the rated speed under the rated load using the proposed method. Throughout the acceleration process, the torque T_e is well kept at its reference and the rotor speed increases smoothly. As seen from the envelope of three-phase stator current, there are no current spikes or oscillations. During the transition of PWM schemes, the proposed method effectively eliminates phase errors, achieving precise synchronization between the phase of the voltage command and the predetermined sampling positions of SSVM.

Fig. 15 shows the spectrum analysis of stator current under BBCS_11 with the prior method and the proposed MPFC. Both methods can achieve symmetrical voltage pulses under steady state. The noninteger and even-order harmonic components are nearly zero, indicating that the proposed MPFC can retain harmonic characteristic of SSVM as that of the prior method.

VI. Conclusion

This article proposes an SSVM-based MPFC for IM drives operating under low switching frequency. To achieve synchronization between the angle of the voltage command and the preset sampling positions, a phase synchronization scheme by adjusting the sampling period is developed for MPFC. The solution of the sampling period compensation value is analytically derived. The proposed method can prevent the phase synchronization error during transient processes in theory, while the prior method can only act as a remedy after the phase error occurs. Moreover, no parameter tuning is required for the proposed phase synchronization, which is favorable for practical application. Simulation and experimental tests were carried out to validate the effectiveness of the proposed method. The results show that the proposed method works well with SSVM. Smooth PWM mode transition, fast phase synchronization and quick dynamic responses are achieved.

Appendix

Letting $\angle \boldsymbol{u}_{\mathrm{s}}^{\mathrm{ref}}$ equal to a sampling position θ_{r}, i.e., $\angle \boldsymbol{u}_{\mathrm{s}}^{\mathrm{ref}} = \theta_{\mathrm{r}}$, the following equation can be obtained according to (30):

$$\frac{\sin(\theta_{\mathrm{r}})}{\cos(\theta_{\mathrm{r}})} = \frac{\psi_{\mathrm{s}}^{\mathrm{ref}} \sin\left(\angle \boldsymbol{\psi}_{\mathrm{s0}}^{\mathrm{ref}} + \Delta\theta\right) - \psi_{\mathrm{s}\beta}^{k+1}}{\psi_{\mathrm{s}}^{\mathrm{ref}} \cos\left(\angle \boldsymbol{\psi}_{\mathrm{s0}}^{\mathrm{ref}} + \Delta\theta\right) - \psi_{\mathrm{s}\alpha}^{k+1}}. \tag{37}$$

Equation (37) can be rearranged as

$$\begin{aligned} &\sin(\theta_{\mathrm{r}}) \cos\left(\angle \boldsymbol{\psi}_{\mathrm{s0}}^{\mathrm{ref}} + \Delta\theta\right) - \cos(\theta_{\mathrm{r}}) \sin\left(\angle \boldsymbol{\psi}_{\mathrm{s0}}^{\mathrm{ref}} + \Delta\theta\right) \\ &= \frac{\psi_{\mathrm{s}\alpha}^{k+1} \sin(\theta_{\mathrm{r}}) - \psi_{\mathrm{s}\beta}^{k+1} \cos(\theta_{\mathrm{r}})}{\psi_{\mathrm{s}}^{\mathrm{ref}}}. \end{aligned} \tag{38}$$

The first row of (38) can be simplified as

$$\begin{aligned} &\sin(\theta_{\mathrm{r}}) \cos\left(\angle \boldsymbol{\psi}_{\mathrm{s0}}^{\mathrm{ref}} + \Delta\theta\right) - \cos(\theta_{\mathrm{r}}) \sin\left(\angle \boldsymbol{\psi}_{\mathrm{s0}}^{\mathrm{ref}} + \Delta\theta\right) \\ &= \sin\left(\theta_{\mathrm{r}} - \Delta\theta - \angle \boldsymbol{\psi}_{\mathrm{s0}}^{\mathrm{ref}}\right). \end{aligned} \tag{39}$$

Based on (38) and (39), the $\Delta\theta$ can be solved as

$$\Delta\theta = \theta_{\mathrm{r}} - \angle \boldsymbol{\psi}_{\mathrm{s0}}^{\mathrm{ref}} - \operatorname{asin}\left(\frac{\boldsymbol{\psi}_{\mathrm{s}}^{k+1} \otimes e^{j\theta_{\mathrm{r}}^{k+1}}}{\psi_{\mathrm{s}}^{\mathrm{ref}}}\right). \tag{40}$$

As $\Delta\theta = \omega_{\mathrm{e}} t_{\mathrm{c}}^{k+1}$, t_{c}^{k+1} can be easily derived from (40) as

$$t_{\mathrm{c}}^{k+1} = \frac{\theta_{\mathrm{r}} - \angle \boldsymbol{\psi}_{\mathrm{s0}}^{\mathrm{ref}} - \operatorname{asin}\left(\frac{\boldsymbol{\psi}_{\mathrm{s}}^{k+1} \otimes e^{j\theta_{\mathrm{r}}^{k+1}}}{\psi_{\mathrm{s}}^{\mathrm{ref}}}\right)}{\omega_{\mathrm{e}}}. \tag{41}$$

References

[1] J. Riedemann et al., "A space vector modulation strategy for PMSMs operating at low switching-to-fundamental frequency ratio," *IEEE Trans. Ind. Electron.*, vol. 70, no. 11, pp. 11067–11077, Nov. 2023.

[2] J. Holtz, "Advanced PWM and predictive control–An overview," *IEEE Trans. Ind. Electron.*, vol. 63, no. 6, pp. 3837–3844, Jun. 2016.

[3] Q. Wang, S. Yang, Z. Xie, X. Zhang, and L. Chang, "Analysis and improvement of synchronous PWM-based closed-loop current control for machine drive," *IEEE Trans. Power Electron.*, vol. 39, no. 8, pp. 10166–10176, Aug. 2024.

[4] A. Birth, T. Geyer, H. d. T. Mouton, and M. Dorfling, "Generalized three-level optimal pulse patterns with lower harmonic distortion," *IEEE Trans. Power Electron.*, vol. 35, no. 6, pp. 5741–5752, Jun. 2020.

[5] G. Narayanan and V. Ranganathan, "Extension of operation of space vector PWM strategies with low switching frequencies using different overmodulation algorithms," *IEEE Trans. Power Electron.*, vol. 17, no. 5, pp. 788–798, May 2002.

[6] M. Ahmed et al., "General mathematical solution for selective harmonic elimination," *IEEE J. Emerg. Sel. Topics Power Electron.*, vol. 8, no. 4, pp. 4440–4456, Apr. 2020.

[7] Z. Zhang, X. Ge, Z. Tian, X. Zhang, Q. Tang, and X. Feng, "A PWM for minimum current harmonic distortion in metro traction PMSM with saliency ratio and load angle constrains," *IEEE Trans. Power Electron.*, vol. 33, no. 5, pp. 4498–4511, May 2018.

[8] C. Wang, Q. Zhang, W. Yu, and K. Yang, "A comprehensive review of solving selective harmonic elimination problem with algebraic algorithms," *IEEE Trans. Power Electron.*, vol. 39, no. 1, pp. 850–868, Jan. 2024.

[9] L. Diao, J. Tang, P. C. Loh, S. Yin, L. Wang, and Z. Liu, "An efficient DSP-FPGA-based implementation of hybrid pwm for electric rail traction induction motor control," *IEEE Trans. Power Electron.*, vol. 33, no. 4, pp. 3276–3288, Apr. 2018.

[10] A. Birda, J. Reuss, and C. M. Hackl, "Simple fundamental current estimation and smooth transition between synchronous optimal PWM and asynchronous SVM," *IEEE Trans. Ind. Electron.*, vol. 67, no. 8, pp. 6354–6364, Aug. 2020.

[11] J. Holtz and N. Oikonomou, "Estimation of the fundamental current in low-switching-frequency high dynamic medium-voltage drives," *IEEE Trans. Ind. Appl.*, vol. 44, no. 5, pp. 1597–1605, May 2008.

[12] S. Dai, J. Wang, Z. Sun, and E. Chong, "Mode transition of synchronous optimal modulation for high-speed PMSM drives," *IEEE Trans. Ind. Appl.*, vol. 58, no. 2, pp. 2001–2012, Mar. 2022.

[13] G. Narayanan and V. T. Ranganathan, "Two novel synchronized bus-clamping PWM strategies based on space vector approach for high power drives," *IEEE Trans. Power Electron.*, vol. 17, no. 1, pp. 84–93, Jan. 2002.

[14] J.-S. Kim, D.-H. Kim, J.-H. Lee, and J.-S. Lee, "Smooth pulse number transition strategy considering time delay in synchronized SVPWM," *IEEE Trans. Power Electron.*, vol. 38, no. 2, pp. 2252–2261, Feb. 2023.

[15] H. Yang, Y. Zhang, G. Yuan, P. D. Walker, and N. Zhang, "Hybrid synchronized PWM schemes for closed-loop current control of high-power motor drives," *IEEE Trans. Ind. Electron.*, vol. 64, no. 9, pp. 6920–6929, Sep. 2017.

[16] L. Xiao, J. Li, Y. Xiong, J. Chen, and H. Gao, "Strategy and implementation of harmonic-reduced synchronized SVPWM for high-power traction machine drives," *IEEE Trans. Power Electron.*, vol. 35, no. 11, pp. 12457–12471, Nov. 2020.

[17] J. Rodriguez et al., "Latest advances of model predictive control in electrical drives–part I: Basic concepts and advanced strategies," *IEEE Trans. Power Electron.*, vol. 37, no. 4, pp. 3927–3942, Apr. 2022.

[18] T. Geyer and D. E. Quevedo, "Performance of multistep finite control set model predictive control for power electronics," *IEEE Trans. Power Electron.*, vol. 30, no. 3, pp. 1633–1644, Mar. 2015.

[19] T. Geyer, N. Oikonomou, G. Papafotiou, and F. Kieferndorf, "Model predictive pulse pattern control," *IEEE Trans. Ind. Appl.*, vol. 48, no. 2, pp. 663–676, Feb. 2012.

[20] H. Yang, Y. Zhang, and M. Li, "Duty-cycle correction-based model predictive current control for PMSM drives fed by a three-level inverter with low switching frequency," *IEEE Trans. Power Electron.*, vol. 38, no. 6, pp. 6841–6850, Jun. 2023.

[21] C. Tang et al., "Low-carrier-ratio model predictive control for 100 khz large-signal multiphase converters with low thd," *IEEE Trans. Power Electron.*, vol. 39, no. 2, pp. 2420–2431, Feb. 2024.

[22] Y. Wang, Y. Zhang, H. Yang, and J. Rodriguez, "Variable-vector-based model predictive control with reduced current harmonic and controllable switching frequency for PMSM drives," *IEEE Trans. Power Electron.*, vol. 39, no. 12, pp. 16429–16441, Dec. 2024.

[23] Y. Zhang and H. Yang, "Model predictive torque control of induction motor drives with optimal duty cycle control," *IEEE Trans. Power Electron.*, vol. 29, no. 12, pp. 6593–6603, Dec. 2014.

Haitao Yang (Member, IEEE) received the B.S. degree from the Hefei University of Technology, Hefei, China, in 2009, the M.S. degree from the North China University of Technology, Beijing, China, in 2015, and the Ph.D. degree from the University of Technology Sydney, Sydney, Australia, in 2020, all in electrical engineering.

He is currently an Associate Professor with the North China University of Technology. His research interests include control of motor drives and PWM converters.

Jiachen Xu was born in Huaian, Jiangsu, China, in March 1997. He received the M.S. degree in electrical engineering from the North China University of Technology, Beijing, China, in 2024.

His research interests include power electric machine drives, model predictive flux control, synchronous PWM, and induction motor.

Shuo Ma was born in Langfang, Hebei, China, in April 1999. He received the B.S. degree in electrical engineering and automation from the Hebei University of Technology, Tianjin, China, in 2021. He is currently working toward the M.S. degree in electrical engineering with the North China University of Technology, Beijing, China.

His current research interests include sensorless control and predictive control of PMSM drives.

Yongchang Zhang (Fellow, IEEE) received the B.S. degree from Chongqing University, Chongqing, China, in 2004, and the Ph.D. degree from Tsinghua University, Beijing, China, in 2009, both in electrical engineering.

From 2009 to 2011, he was a Postdoctoral Fellow with the University of Technology Sydney, Ultimo, NSW, Australia. He was as an Associate Professor with the North China University of Technology, Beijing, in 2011, and was promoted to a Full Professor in 2015. Since 2021, he has been a Full Professor with North China Electric Power University, Beijing. He has authored or coauthored more than 100 technical papers in the area of motor drives, pulsewidth modulation, and ac/dc converters. His current research focuses on the model predictive control for power converters and motor drives.

Dr. Zhang is a Fellow of the Institute of Engineering and Technology. He was the Technical Program Co-Chair of 5th/6th/7th IEEE International Conference on Predictive Control of Electrical Drives and Power Electronics. He serves as the Editor and Associate Editor for several international journals, such as IEEE JOURNAL OF EMERGING AND SELECTED TOPICS IN POWER ELECTRONICS, IEEE TRANSACTIONS ON ENERGY CONVERSION, and IEEE TRANSACTIONS ON INDUSTRY APPLICATIONS.